Tropospheric Age-of-Air: Influence of SF_6 Emissions on Recent Surface Trends and Model Biases

Clara Orbe[1], Darryn W. Waugh[2], Stephen Montzka[3], Edward J. Dlugokencky[3], Susan Strahan[4,5], Stephen D. Steenrod[4,5], Sarah Strode[4,5], James W. Elkins [3,7], Bradley Hall [3], Colm Sweeney [3], Eric J. Hinsta [3,6], Fred L. Moore [3,6], Emma Penafiel [2]

[1]NASA Goddard Institute for Space Studies, New York, NY, USA
[2]Department of Earth and Planetary Sciences, Johns Hopkins University, Baltimore, MD, USA
[3]Global Monitoring Laboratory, NOAA, Boulder, CO, USA
[4]Universities Space Research Association, Columbia, MD, USA
[5]Atmospheric Chemistry and Dynamics Laboratory, NASA Goddard Space Flight Center, Greenbelt, MD, USA
[6]Cooperative Institute for Research in Environmental Sciences (CIRES), University of Colorado Boulder, Boulder, CO 80309, USA
[7]Currently retired

Key Points:

- The mean age since air was last at the NH midlatitude surface features large (small) meridional gradients in the tropics (extratropics).
- Recent mean age trends in the SH, estimated from measurements of SF_6, likely reflect shifts in SF_6 emissions, not transport changes.
- Modeled SF_6 ages in the SH are older than observed, partly due to overestimation in simulated SF_6 mixing ratios near NH emissions regions.

Corresponding author: Clara Orbe, `clara.orbe@nasa.gov`

Abstract

The mean age since air was last at the Northern Hemisphere (NH) midlatitude surface is a fundamental property of tropospheric transport. Here we approximate the mean age in terms of an "SF_6 age" (Γ_{SF6}), derived from surface and aircraft measurements of SF_6 that are broader in spatial scope and cover a longer time period (1997-2018) than considered previously. At the surface, Γ_{SF6} increases from near-zero values north of 30°N to ∼1.5 years over the Southern Hemisphere (SH) extratropics, with the largest meridional gradients occurring in the tropics. By comparison, vertical gradients in Γ_{SF6} are weak throughout, with only slight increases/decreases with height in the NH/SH. The broader spatial coverage of the measurements reveals strong variations in the seasonal cycle of Γ_{SF6} within the (sub)tropics that are weaker over the Atlantic and Pacific oceans, compared to over the Indian Ocean.

Observations from 2000-2018 reveal that the SF_6 age at sites in the SH has been decreasing by ∼0.12 yr/dec. However, this decrease is not due to changes in transport but, rather, is likely related to changes in emissions, which have increased globally and reportedly shifted from northern midlatitudes into the subtropics. Simulations, which reproduce the SF_6 age trends, show no decreases in an age-of-air tracer, reinforcing the fact that Γ_{SF6} represents only an approximation to the mean age. Finally, the modeled SF_6 ages are older than observed, by ∼0.3-0.4 years throughout the southern extratropics. We show that this bias is partly related to an overestimation in simulated SF_6 near emissions regions, likely reflecting a combination of uncertainties in emissions and model transport.

Plain Language Summary

The mean age since air was last at the Northern Hemisphere midlatitude surface is a fundamental timescale of tropospheric transport. The mean age is not directly observable, but can be estimated from measurements of SF_6 to derive an "SF_6 age" (Γ_{SF6}), or the time lag since the SF_6 mixing ratio at a given location equaled the mixing ratio over a northern midlatitude source region. Here we use new surface and aircraft measurements of SF_6 to construct an estimate of the mean age that covers a longer period (1997-2018) and is more globally resolved, compared to previous estimates. The broader spatial coverage reveals strong variations in the seasonal cycle of Γ_{SF6} within the (sub)tropics that are weaker over the Atlantic and Pacific oceans, compared to over the Indian Ocean. The longer temporal record also reveals that Γ_{SF6} has been decreasing by ∼0.12 yr/dec. Quite importantly, this decrease is not due to underlying changes in transport but, rather, is likely related to changes in SF_6 emissions, which increase globally while shifting from northern midlatitudes into the subtropics. We also show that the longstanding old bias in modeled Γ_{SF6} is partly related to an overestimation in simulated SF_6 near emissions regions.

1 Introduction

The mean time since air last contacted the midlatitude surface layer of the Northern Hemisphere (NH) – the mean age from the NH surface (Waugh et al. (2013)) – is a fundamental measure of troposphere transport. Unlike more conventional global metrics, like the hemispherically integrated interhemispheric exchange time (e.g., Levin and Hesshaimer (1996); Geller et al. (1997)), the mean age provides a much richer (three-dimensional) description of interhemispheric transport (IHT).

Similar to the mean age in the stratosphere (Kida (1983); T. Hall and Plumb (1994)), the mean age from the NH surface provides an integrated measure of transport that reflects both advection by the meridional circulation and mixing across transport "barriers". The age considered here, however, refers to transport from the NH midlatitude surface, in contrast to the tropical tropopause used to define the stratospheric mean age, or to the entire Earth's surface (e.g., the "tropospheric age of air" (Patra et al. (2009))).

The mean age is not directly observable, but can be estimated from measurements of SF_6 to derive an "SF_6 age" (Γ_{SF6}), or the time lag since the SF_6 mixing ratio at a given location equaled the mixing ratio over a northern midlatitude source region. Using a combination of ship and ground-based as well as in-situ aircraft measurements of sulfur hexafluoride (SF_6) Waugh et al. (2013) showed that Γ_{SF6}, is characterized by values that increase sharply from zero over northern midlatitudes to ∼1.3-1.5 years over the Southern Hemisphere (SH). They also showed that the largest seasonal and interannual variations occur over the tropics and near the surface, and are relatively weaker in the extratropics and upper troposphere.

The observational inferences of Γ_{SF6} derived in Waugh et al. (2013) provide stringent tests of simulated transport, independent of photochemistry, and have been used to evaluate interhemispheric transport in models (Waugh et al. (2013); Wu et al. (2018); Orbe et al. (2018); Yang et al. (2019)). In particular, the analyses of individual models presented in Waugh et al. (2013) and Wu et al. (2018) showed that the simulated ages were biased old, relative to observations. This bias was subsequently shown to apply more generally across all models participating in the Chemistry Climate Modeling Initiative (CCMI) (Eyring et al. (2013)) and TransCom (Patra et al. (2011)) model intercomparisons (Yang et al. (2019)).

In order to meaningfully interpret the age biases in models, more observations are needed in order to better understand the observed spatial and temporal characteristics of Γ_{SF6}. In particular, the observational analysis in Waugh et al. (2013) was limited to a relatively narrow (in longitude) network of measurements centered around the Pacific Ocean (see their Figure 1), which precluded an in-depth examination of the zonal characteristics of the mean age (and its variability). While previous studies have documented zonal variations in the observed interhemispheric transport of other trace gases (most commonly, CO_2), focus has primarily been placed on the upper troposphere, where asymmetries in transport have either been linked to the presence of upper-level westerly ducts in the Pacific and Atlantic Oceans (e.g. Miyazaki et al. (2008); Frederiksen and Francey (2018)) or to the upper-level cross equatorial flow associated with the Asian monsoon anticyclone (e.g., Chen et al. (2017); Yan et al. (2020)). By comparison, less attention has been paid to examining zonal variations in IHT in the lower troposphere, although modeling studies do suggest the presence of longitudinally confined cross-equatorial transport paths over South America and the Indian Ocean (Orbe et al. (2016); Wu et al. (2018)). Most relevant to this study, Wu et al. (2018) showed that near-surface values of Γ_{SF6} exhibit considerable differences in variability between the Indian Ocean and the Pacific, although that study was mainly model-based and did not expand on the observational analysis presented in Waugh et al. (2013).

In addition to being limited to one ocean basin, the observational analysis of Γ_{SF6} presented in Waugh et al. (2013) only spanned 1997-2011, too short to justify an analysis of age trends. At the same time, however, studies using different approaches have concluded that interhemispheric transport did change over that time period, with Patra et al. (2011) showing that the observed interhemispheric exchange time decreased by about ∼0.2 years during 1996–1999 and ∼0.15 years during 2004–2007. While they suggest that these decreases in exchange time are likely driven by changes in the emission distribution of SF_6, it is not clear if such trends are also evident in the three-dimensionally resolved mean age. Furthermore, recent emissions inventories suggest that the expansion in SF_6 consumption moving from developed (Kyoto Protocol Annex-1) to developing countries (non-Annex-1) has increased still further over the past decade (Simmonds et al. (2020); Lan et al. (2020)) and it is not clear how (if) these emissions changes contribute to sustained recent trends in inferred rates of interhemispheric transport.

Here we use the full network of surface SF_6 measurements from the NOAA Carbon Cycle Greenhouse Gases (CCGG) group that is much broader in its zonal coverage compared to previous studies and extends over the time period 1997-2018 in order to evaluate zonal variations in the mean age and its long-term trends over the past two decades. Combining the surface measurements with new in-situ aircraft measurements sampled during the Atmospheric Tomography Mission (ATom) we show that, while there are weak zonal asymmetries in the annual mean ages, the amplitude of the seasonal cycle of Γ_{SF6} is much larger over the Indian Ocean/Maritime Continent compared to over the Pacific and Atlantic Oceans.

Our analysis of the full period spanning 1997-2018 reveals that the SF_6 age has decreased nearly uniformly throughout the 2000s at a rate of ∼0.12 yr/dec. We then use model simulations to show that this trend is mainly associated with a shift in emissions, as diagnosed from the Emission Database for Global Atmospheric Research (EDGAR) inventory, from northern to subtropical latitudes and is not, to first order, related to trends in transport through the tropics. Finally, we show that the model simulates substantially larger spatial variance in the SF_6 mole fraction over northern midlatitudes, compared to the observations. We then show that the long-standing age bias documented in previous studies is largely, but not entirely, traceable to this larger simulated spatial variance over northern midlatitudes in the models.

We begin by discussing the observations and model simulations that were used in Section 2, followed by a presentation of main results in Sections 3 and 4 and conclusions in Section 5.

2 Methods

2.1 Observations

Here we use the monthly mean flask-air measurements from the NOAA/CCGG division, which makes regular SF_6 measurements from discrete samples going back to 1997, depending on the site (Figure 1, black squares). The monthly mean flask-air measurements are calculated from a smooth curve fitted to the data, which includes approximately four weekly samples per month. Unlike in Waugh et al. (2013), who only used NOAA/CCGG measurements from tropical sites and commercial ship-based measurements over the Pacific Ocean, here we consider a much broader range of (82) NOAA/CCGG sites that also span the extratropics and multiple ocean basins.

The quoted uncertainty for the NOAA/CCGG measurements is ∼0.04 ppt in years since the early 2000s, during which the total measurement uncertainty is dominated by short term noise. These uncertainties translate to age uncertainties of approximately 0.13 yr, assuming an SF_6 growth rate of around 0.3 ppt/yr. For years prior to 2000, we note that there is an additional uncertainty contribution due to standard scale propagation which increases the total measurement uncertainty to ∼0.07 ppt. For this reason, when examining trends in the surface data, we exclude years before 2000 from our analysis.

In addition to the surface measurements, we also use the SF_6 measurements sampled on the NASA DC-8 aircraft during the Atmospheric Tomography Mission (ATom). ATom consisted of four aircraft campaigns that provided continuous profiles from 0.2 to 12 km that originated from California, flew north to the western Arctic and south into the South Pacific, and east to the Atlantic up to northern Greenland before returning back to California (Fig. 1, open circles). The merged datasets from all four campaigns – ATom-1 (Jul-Aug 2016), ATom-2 (Jan-Feb 2017), ATom-3 (Sep-Oct. 2017) and ATom-4 (Apr-May 2018) – are used. Specifically, we use the 10 second merged SF_6 in-situ chromatographic measurements from the PAN and Other Trace Hydrohalocarbon Experiment (PANTHER) (J. W. Elkins et al. (2002); Wofsy (2011)) and the Unmanned Aircraft Systems Chromatograph for Atmospheric Trace Species (UCATS) (J. Elkins et al.

(1996); Moore et al. (2003); Fahey et al. (2006); B. Hall et al. (2011); Wofsy (2011)) instrument. We also use the Programmable Flask Package (PFP) Whole Air Sampler merged data, which is obtained less frequently as integrated samples over longer time intervals (<30s) and is available as (weighted) averages of 1-second data.

The stated uncertainty for the PFP measurements is around 0.05 ppt and, while the UCATS and PANTHER reported values vary across the 3-4 deployments for which measurements were available, on average their reported uncertainty is around 0.08 ppt (Table 1, col. 2-4). These reported uncertainties compare well with the standard deviation of the difference between instruments sampled for coincident measurements (within 70 sec). That is, assuming that the uncertainties in two instruments X and Y are uncorrelated, then σ^2(X-Y) = σ^2(X)-σ^2(Y). Evaluating this variance in the difference between co-incident SF_6 measurements results in values (i.e. σ(PFP-UCATS)=0.09 and σ(PANTHER-UCATS)=0.11) that are (broadly) consistent with the reported uncertainties (Table 1, col. 5-7). Not only is the spread in the measurements generally consistent in magnitude with the reported uncertainties, we also find that the larger spread for campaigns also coincides with larger reported uncertainties (e.g. campaigns 1 and 4 for UCATS, and campaign 4 for PANTHER). This relationship has been evaluated and shown to hold well over the Southern Hemisphere (not shown).

Assuming an SF_6 growth rate (during AToM) of around 0.3 ppt/yr, then the uncertainties in the PFP (0.05 ppt) and UCATS/PANTHER (0.08 ppt) measurements translate to age uncertainties associated with an individual measurement of approximately 0.16 yr and 0.26 yr, respectively.

2.2 Models

We use two simulations produced using the NASA Global Modeling Initiative (GMI) chemical transport model (Strahan et al. (2007, 2016)). Both simulations span 1980-2016 and are constrained with fields from the Modern-Era Retrospective Analysis for Research and Applications, Version 2 (MERRA-2) (Gelaro et al. (2017)). While the simulations differ in their horizontal resolution (one- vs. two-degree), the primary difference is in their emissions. In the first simulation, denoted "CTM-Fix", the emissions are identical to those used in Waugh et al. (2013) and are based on the EDGAR 2000 inventory using the temporal scaling factors in Table 2 of Levin et al. (2010) (assuming a constant scaling after 2008) (Fig. 2a). In the second CTM simulation, hereafter simply "CTM", the emissions are from EDGAR v4.2 (2011) and thus capture a substantial shift in SF_6 emissions from northern midlatitudes, over Europe and the United States, into the subtropics over Asia during 1997-2007 (Fig. 2b). The emissions pattern from 2008 is used for years after 2008, the last year of the EDGAR v4.2 inventory.

2.3 SF_6 age

As in Waugh et al. (2013) we focus primarily on the "SF_6 age" (Γ_{SF6}) derived from both the observed and modeled SF_6 fields. More precisely, the age at a particular location, Γ_{SF6}(r), is defined as the time since the SF_6 mixing ratio in the "source region" equaled the mixing ratio at that location, i.e., ($\chi(\mathrm{r},\mathrm{t}) = \chi_0(\mathrm{t}-\Gamma_{SF6}(\mathrm{r},\mathrm{t}))$), where χ is the SF_6 mixing ratio at location r and χ_0 is the mixing ratio in the (northern midlatitude) source region.

In defining Γ_{SF6} one must choose a suitable reference time series, χ_0. In Waugh et al. (2013) the authors used the average of three northern midlatitude sites, Mace Head (MHD; 53°N,10°W), Trinidad Head (THD; 41°N,124°W), and Niwot Ridge (NWR; 40°N,106°W) from the NOAA Halocarbons and other Atmospheric Trace Species (HATS) network. Here we capitalize on the much broader network of NOAA/CCGG sites included in this study and define a boundary condition (BC) ($[\chi]_{0,30\mathrm{N}-60\mathrm{N}}$) which uses the mean of measured SF_6 mole fractions at all (31) available sites spanning 30°N to 60°N.

As discussed in more detail in Section 4, this choice of a mean reference series, while consistent in form with the one used in Waugh et al. (2013) (in terms of averaging), adds an additional layer of complexity when comparing between the observations and the model, as compared to using the median of the sites ($<\chi>_{0,30\mathrm{N}-60\mathrm{N}}$). This is because the mean is more influenced by stations near emissive regions, and this influence is typically enhanced in the model, compared to the observations. This results in a model reference time series with higher values which, for a given SF_6 mixing ratio, translates to older ages outside of NH midlatitudes. While the high SF_6 sites in the model results presented in this study represent a real model bias over that region, the median reference series is used when comparing the model with the observations in Section 4, as the focus of that section resides primarily in what the SF_6 age reveals about interhemispheric transport (not local transport in close proximity to the northern midlatitude source region).

Finally, in addition to analyzing the SF_6 age we also briefly include comparisons with an idealized NH "age-of-air" clock tracer, which is shown only for the "CTM" simulation as it is nearly identical in both runs (not shown). The clock tracer is defined with respect to a uniform source over 30°N–50°N and was compared among the CCMI models in Orbe et al. (2018). This tracer is used for discerning the relative influence of emissions versus transport changes on recent trends in Γ_{SF6}.

2.4 Analysis

We examine the climatological mean of Γ_{SF6}, as well as its seasonal and interannual changes. Seasonality is examined at each grid point both in terms of the peak-to-peak amplitude in the climatological mean seasonal cycle as well as by calculating the standard deviation of the climatological 12-month annual cycle over the entire observational period 1997-2018 (denoted as σ^{seas}). Similarly, the interannual variability (σ^{inter}) is examined by calculating the standard deviation at each given month over the same period. Note that there is a trend in Γ_{SF6} present over this time period, which is quantified herein using a simple linear fit and which is removed first before calculating interannual variations. This last step was not performed in the model-based analysis of Γ_{SF6} presented in Wu et al. (2018) as that study only considered Γ_{SF6} variability up to 2010, over which the age trend is smaller.

3 Observed Tropospheric SF_6 Ages

3.1 Climatological Mean Distribution

We begin by examining the SF_6 age (Γ_{SF6}) as a function of latitude, evaluated at all of the NOAA/CCGG sites (Figure 3). Despite the use of a reference time series that considers a much broader range of sites than examined in Waugh et al. (2013), we find a meridional profile that is very consistent with what was reported in that earlier study (see their Figure 3). In particular, the SF_6 ages are near zero (by construction) over the NH midlatitude source region and increase sharply in the northern subtropics and tropics, where the ages feature large meridional gradients, increasing to a value of ∼1.5 years over southern middle and high latitudes.

Whereas the analysis in Waugh et al. (2013) focused primarily on ages over the Pacific Ocean, here we examine the variations in Γ_{SF6} over a much broader range of longitudes (Fig. 4a). South of the source region throughout the tropics and SH latitudes we find that there are small zonal variations in the climatological annual mean SF_6 ages. Over the northern subtropics and close to the source region there are larger asymmetries in the age, with younger ages occurring near regions of high emissions and several sites where Γ_{SF6} is negative. Waugh et al. (2013) made a similar observation, which they explained as resulting from the inclusion of the higher altitude NWR data in their (three-site) reference time series. By comparison, in this study, which utilizes a boundary condition formed from sites that cover a broader range of longitudes, we find that these negative ages coincide with sites located in regions of high emissions over Europe (-0.24 yr. at HUN (47°N,17°E)), Southeast (SE) Asia (-0.32 yr. at TAP (37°N,126°E)), and the Pacific Ocean (-0.5 yr. at DSI (21°N,117°E)) (circles, Fig. 4a). As discussed later in Section 3.3, changes in SF_6 emissions near these low-age sites dictate to a large extent the trends in Γ_{SF6} that occur over the tropics and southern latitudes during the 2000s.

Next we examine the SF_6 ages inferred from ATom over the period 2016-2018 (Figure 4b-d). In particular, the ages, sampled at pressures greater than 400 hPa, have been binned into a 10° longitude by 5° latitude grid for the UCATS and PANTHER instruments and into a 15° longitude by 10° latitude grid for PFP, owing to the relatively coarser temporal sampling of the latter. Overall, there is good agreement between the ages inferred from the different instruments, which all show consistently weak zonal variations in Γ_{SF6} across oceanic basins. Most differences among instruments fall within the ∼0.16 yr and ∼0.26 yr age uncertainties expected for PFP and UCATS/PANTHER, respectively. While there are a few exceptions where the age differences are larger than expected, we find that these reflect locations where the sampling density is small; furthermore, in practice, they comprise only a small fraction of the measurements.

Overall we find that the SF_6 ages inferred from ATom appear to also agree very well with the NOAA/CCGG-based surface ages (Fig. 4a), albeit for the different climatological time periods considered. In particular, the ages inferred from ATom also feature weak zonal variations, with little differences between the Pacific, Atlantic and Indian Oceans.

One exception to this good agreement, however, occurs over the northern hemisphere middle and high latitudes, where Γ_{SF6} ∼0.3-0.6 yr in ATom, compared to only ∼0.1-0.3 yr at the surface. This difference is due to a small increase in Γ_{SF6} with height over northern midlatitudes (Figure 5). In particular, over 50°N-70°N the ATom-inferred ages increase from ∼0.2 yr at the surface to ∼0.4-0.5 yr at 300 hPa, a feature that is evident in all three instruments (Fig. 5a). A similar (albeit smaller) increase in Γ_{SF6} with height appears over southern high latitudes (Fig. 5b), a feature that was also evident in the aircraft-based age estimates presented for the Pacific Ocean in Waugh et al. (2013). Physically, we interpret these increased ages in the upper troposphere as reflecting a decrease in tropopause height and increased sampling of lower stratospheric air masses, which in future work we plan to examine further in terms of reductions and elevations in nitrous oxide and ozone, respectively.

By comparison, over the tropics the vertical gradients in Γ_{SF6} are much weaker (Fig. 5c,d), and increase only slightly moving into southern high latitudes. These weak vertical gradients in the tropics are evident in both the Pacific (Fig. 5c) and Atlantic (Fig. 5d) basins, consistent with the weak surface zonal asymmetries in the annual mean ages inferred from the surface measurements (Fig. 3).

3.2 Seasonal and Interannual Variability

Having shown in the previous section that there is generally very little vertical variation in the age over the regions sampled during ATom (except over northern and southern high latitudes), we focus the remainder of our discussion on variability and trends at the surface. We begin by examining seasonal variations in the age (σ^{seas}) (Fig. 6a), which are largest over the tropics and northern subtropics. Within the tropics the standard deviation across the seasonal cycle ranges between ∼20 days and ∼120 days (or almost 0.3 years) (Fig. 6, left, top).

Examination of the seasonal cycle at individual sites over different regions (Figure 7) shows considerable zonal variability in the amplitude of the seasonal cycle, in contrast to the relatively small variations in the climatological annual mean ages noted in the previous section. More precisely, for sites located south of 20°N, the largest seasonal variations in Γ_{SF6} occur over the Indian Ocean (Fig. 7b), with relatively weaker variability over the Pacific Ocean (Fig. 7c) and still weaker seasonality over the Atlantic Ocean (Fig. 7d). Overall, the peak-to-peak amplitudes over the Indian Ocean range between 0.7 yr and 1.4 yr, compared to ∼0.6 yr and ∼0.3 yr over the Pacific and Atlantic, respectively.

The large differences in σ^{seas} between the Indian Ocean and the other basins reflect the fact that the seasonality of Γ_{SF6} is not a simple function of distance from the equator. In particular, at the same latitude (∼5°S) the amplitude of the seasonal cycle is much larger over the Indian Ocean (BKT (0.2°S,100°E), SEY (4.7°S,56°E)) compared to the Pacific (PCS05; 5°S,165°W). As noted in Waugh et al. (2013), the seasonal cycle in Γ_{SF6} at these tropical sites reflects the fact that older ages occur during summer as the Intertropical Convergence Zone (ITCZ) shifts northward, bringing in older SH ages into that region; conversely, during boreal winter the ITCZ shifts into the SH and the ages, of NH origin, are relatively younger. The larger seasonal variations at SEY therefore reflect the fact that the seasonal variations in the latitude of the ITCZ are larger than at the longitudes of other (Pacific) sites. While we find that this argument also qualitatively applies to the Indian Ocean site BKT (not considered in Waugh et al. (2013)), we note that this is only part of the story as Wu et al. (2018) later showed that the ITCZ-age relationship differs between the basins, with the relationship being much less linear over the Indian Ocean, with a more rapid change of age with latitude of the ITCZ when the ITCZ is south of 10°N versus north.

The amplitude of interannual variability (σ^{inter}), averaged over all months and inferred from the NOAA/CCGG observations, is similar to the seasonal cycle amplitude, albeit somewhat higher over southern latitudes (Fig. 6b). Compared to the seasonal cycle, σ^{inter} is also somewhat more uniform in longitude, with the exception of a few sites located near regions of high emissions.

3.3 Trends

Next, we capitalize on the longer time series afforded from the updated observational record by calculating trends, ignoring years prior to 2000, during which the total measurement uncertainty of the surface flask data was significantly larger. In particular, over 2000-2018 the SF_6 ages decrease south of the northern midlatitude source region (Figure 6c). Over southern extratropical latitudes the trends in Γ_{SF6} are ∼-45(-0.12) days(yrs)/dec (Fig. 6c, top); furthermore, with the exception of some variations close to regions of high emissions (i.e. Europe, SE Asia), the trends in the ages over southern latitudes are overall zonally uniform (Fig. 6c, bottom).

The decreases in Γ_{SF6} are consistent with the results from Patra et al. (2011), as discussed in the Introduction. However, whereas they showed that the interhemispheric exchange time decreases by ∼0.05 years over 1996–2007, here we show that this trend applies more generally to all surface latitudes south of 30°N and over a longer time period extending through 2018.

Patra et al. (2011) suggested that the decreases in exchange time were driven by a subtropical shift in SF_6 emissions. To test whether this hypothesis also applies to the SF_6 age trends over the longer record, we first consider how changes in the reference time series used to calculate Γ_{SF6} (adjusted to in/exclude sites reflecting changes in emissions) affect the resulting age trends.

We begin by noting that, by construction, the changes in Γ_{SF6} summarized in Figure 6, already partly reflect recent changes in the EDGAR SF_6 emission inventory, which shift from northern midlatitudes during the late 1990s and early 2000s to lower latitudes (in Southern Asia) during the mid-2000s and 2010s. That is, the mean 30°N-60°N boundary condition ($[\chi]_{0,30N-60N}$) used to calculate Γ_{SF6}, already averages in the contributions from sites in Northern Europe like HUN — near which emissions have been reportedly decreasing over recent years — and, conversely, sites over SE Asia (TAP,AMY), near which emissions have recently been increasing. As a result, removing HUN from the reference time series results in a new reference series (Figure 8a, cyan line) that differs by ∼0.01 ppt during ∼2000 and by ∼0.025 ppt over more recent years; in turn, this change in the evolution of the reference SF_6 series reduces the amplitude of the resulting (negative) age trend by ∼15% (Fig. 8b, cyan circle).

While, in one sense, one can remove the influence of emissions changes over northern midlatitude sites (HUN), one can, alternatively, remove the contributions from the SE Asian sites (TAP, AMY). We only consider TAP, as that site has measurements for the entire period under consideration. Upon removing the influence of TAP, the resulting reference time series becomes increasingly more negative with time, relative to using the all-site 30°N-60°N mean (Fig. 8a, solid red line); in turn, the negative age trends over southern latitudes become even larger (Fig. 8a, solid red circle).

One can take this exercise one step further by comparing the age trends inferred using the mean 30°N-60°N boundary condition with those from a "marine boundary layer" reference series that only uses sites between 30°N-60°N that are far removed from emissive sources. Consideration of only these marine locations results in a reference time series that becomes increasingly smaller with time by up to ∼0.06 ppt, relative to the 30°N-60°N mean series (Fig. 8a, black line), resulting in negative age trends that are substantially larger (Fig. 8b, open black circle). While it is tempting to interpret this sensitivity in the SF_6 age trends to emissions *shifts*, the stronger trends might simply reflect increasing SF_6 emissions over land that are not captured in the marine BC.

To summarize, the negative SF_6 age trends observed over tropical and southern latitudes become smaller (larger) when we include (exclude) sites near regions with substantial and recently changing emissions into the reference series that is used to calculate Γ_{SF6}. This suggests that recent decreases in Γ_{SF6} are partly related to a reported shift in emissions from northern midlatitudes into more southern latitudes over Southeast Asia. We also find that the Γ_{SF6} trends become substantially larger when we use a marine reference series that only considers sites between 30°N-60°N that are far removed from emissive sources. However, this increase in trends might reflect simply increasing (not necessarily shifting) SF_6 emissions over land. As this demonstration is mainly indirect (through modification of the reference series used to calculate the age) and inconclusive regarding the impact of emissions shifts, we examine more directly the impact of recent emissions changes on age trends through use of targeted model simulations discussed next in Section 4.

4 Modeled SF_6 Ages

To examine possible causes of the reported SF_6 age trends we now compare model simulations that use different SF_6 emissions. Specifically, we use two model simulations, one using emissions that shift in time, and the other using fixed emissions. We also compare the trends in Γ_{SF6} with those derived from the age-of-air "clock" tracer as another means for discerning the relative importance of transport versus emissions on recent observed trends in Γ_{SF6}.

To begin, we provide a brief examination of the simulated climatological mean SF_6. The model simulates much larger spatial variance in SF_6 over northern midlatitudes, compared to the observations (Fig. 9). In particular, both simulations produce higher values of SF_6 over several sites spanning Europe, the United States and Southeast Asia, all of which are located near/downwind of emissions regions. Over some of these sites (HPB (48°N,11°E), OXK (50°N,12°E), PTA (39°N,124°E)) the model also fails to capture the observed seasonal cycle in Γ_{SF6} (Fig. 7a), although these biases in seasonal cycle amplitude appear to be relatively confined to northern midlatitudes and do not propagate south of the source region.

The disagreement between the observed and simulated values of SF_6 over northern midlatitudes is not easy to interpret. In particular, while utilizing only measurements satisfying a certain criterion, such as flow regime, may account for discrepancies with the models at some of the sites, it does not consistently explain the differences between the simulated and observed concentrations across all sites. Therefore, while sampling may play a role in the mismatch between the models and observations, an alternative explanation is that the higher values of SF_6 in the models reflect a tendency for tracer concentrations to be excessively "trapped" near regions of high emissions (Denning et al. (1999); Peters et al. (2004)). The latter could reflect inaccurate emissions distributions in the EDGAR inventory, especially over the United States, where EDGAR may overestimate emissions by ∼40% (Hu et al. (2021)). Alternatively, the higher values of SF_6 could reflect localized biases in transport away from emissions associated with mixing in the planetary boundary layer (Peters et al., 2004) or other processes. At present it is not clear which of these explanations dominates; rather, it is most likely a combination of these effects, which we plan to disentangle in future research.

The high SF_6 at these NH sites has a major impact on the SF_6 age. This is illustrated in Figure 10, where we compare Γ_{SF6}, calculated with respect to the mean (Fig. 10a) versus the median (Fig. 10b) of the sites spanning 30°N-60°N ($[\chi]_{0,30N-60N}$ vs. $<\chi>_{0,30N-60N}$). For the observations the inferred ages agree well at all latitudes, consistent with the lack of strong observed spatial gradients in SF_6 over northern latitudes (Figs. 9,10 black circles). By comparison, in the models, the values of Γ_{SF6} reduce by ∼0.3 years over SH high latitudes when $<\chi>_{0,30N-60N}$ is used as the reference time series (Figs. 9,10 red circles). (Note that only the results from the CTM simulation are shown, but the same sensitivity is exhibited by the CTM-Fix simulation.)

Figure 10 indicates that after better accounting for the bias in SF_6 (spatial) variance over northern midlatitudes, there is substantially better agreement between the observed and simulated SF_6 ages, at least to within the range of interannual variability. Specifically, the model bias over southern high latitudes is reduced by ∼50% from 0.3 years to 0.15 years, comparable to the surface measurement uncertainty (±0.16 years). This finding expands on the hypothesis raised in Yang et al. (2019), who demonstrated that the bias in simulated Γ_{SF6} over the southern extratropics is most sensitive to transport processes between the northern midlatitudes and northern subtropics. That study, however, did not further partition this bias into transport out of the midlatitude surface versus transport from the northern subtropics into the tropics, owing to the use of a simple box model. Here we show that much of this bias appears to be related to transport out of the midlatitude surface layer, although inaccurate emissions distributions may also be an important contributing factor.

Finally, having demonstrated that the models capture the mean (Fig. 10b) and seasonal variability (Fig. 7) of Γ_{SF6}, next we explicitly compare time series over 2000-2018 (Figure 11). We find that the CTM-Fix run, in which SF_6 emissions do not shift in time, does not capture the observed downward trend in Γ_{SF6} over the 2000s. (Note that the observed negative trend in Γ_{SF6} (Fig. 11, black lines) does not depend on whether the mean or median reference series is used to define the age, consistent with relatively weak spatial variance in observed SF_6 over northern midlatitudes (Fig. 9)). By comparison, the CTM simulation, which uses emissions that shift in time, features a distinct decrease in Γ_{SF6} that is more consistent with the observed trend. This directly confirms our conclusion, inferred earlier through modification of the reference time series (Section 3.3), that the SF_6 age trends are largely attributable to a subtropical shift in emissions from northern middle to subtropical latitudes. This point is perhaps still clearer through analysis of the clock tracer (Fig. 11, green line), which does not exhibit any trends over this period. This confirms that any changes in Γ_{SF6} are primarily a reflection of changes in the latitudinal distribution of emissions, and are not related to underlying changes in transport. Furthermore, consistent with the lack of clock tracer changes, we do not identify any significant trends in either the ITCZ position or mean meridional circulation strength inferred from MERRA-2, relative to internal variability, over this time period (not shown).

Interestingly, while the simulation driven with EDGAR v4.2 emissions does capture most of the age decrease over the 2000s, it is clear that the more recent decreases in Γ_{SF6} after 2010 are less well simulated. This is consistent with the fact that the model uses the same (2008) emissions distribution for all years after 2007. By comparison, the continued decline in observed values of Γ_{SF6} indicates that SF_6 emissions have continued to shift into the subtropics, which has also been suggested in independently derived emissions estimates presented in recent studies (Simmonds et al. (2020); Lan et al. (2020)). Current protocols, such as those set forth in CCMI, for evaluating interhemispheric transport using EDGAR v4.2 emissions, may therefore need to be updated in order to properly account for these continued shifts in emissions over recent years.

As a final point, we note that over southern high latitudes the interannual age variability is slightly underestimated in both the CTM and CTM-Fix simulations, even after accounting for the differences in SF_6 spatial variance between the model and the observations (Fig. 11b,c). While this weaker variability does appear to be consistent with the values of σ^{inter} presented in Wu et al. (2018) (for the NCAR CAM model), we do not draw any firm conclusions, given that this apparent bias in σ^{inter} is somewhat dependent on which measurements are used. Furthermore, it is possible that the larger variability in the observations could be due to uncertainty in the measurements, given the limited sampling that occurs for any given month at most sites. At this point, therefore, it is not clear how much of the bias in the models is due to model error or measurement uncertainty. A systematic evaluation of interannual variability in Γ_{SF6} among the broader range of models participating in CCMI will be examined in future work, but is beyond the scope of the present analysis.

5 Conclusions

Here we have used surface and aircraft measurements of SF_6 to present a more global picture of the climatological distribution, recent trends, and variability in the tropospheric SF_6 age. Our analysis, which has focused on the observations, shows that at the surface, the SF_6 age increases from near-zero values north of 30°N to $\sim$1.5 years over the SH extratropics. While the surface meridional gradients in Γ_{SF6} are large in the tropics, they are significantly weaker in the extratropics; moreover, vertical gradients in the age are weak over all latitudes, in(de)creasing only slightly with height over northern(southern) high latitudes. In addition, our use of a more spatially resolved network of surface measurements shows that there are small zonal variations in the climatological annual mean SF_6 ages, albeit large zonal variations in age seasonality, especially over the Indian Ocean.

Unlike previous studies, which did not examine trends in the SF_6 age within the troposphere, here we capitalize on the longer measurement record to show that Γ_{SF6} has decreased nearly uniformly south of northern midlatitudes by $\sim$0.12 yr/dec over 2000-2018. Interestingly, we show that changes in Γ_{SF6} are primarily associated with a change in reported emissions, possibly including a shift from northern midlatitudes into the northern subtropics, and are not related to fundamental changes in transport. In particular, simulations reproducing the observed SF_6 age trends show no corresponding decreases in an age-of-air tracer over this time period, reinforcing our conclusion that the SF_6 age represents only an approximation to the mean age. Thus, while the SF_6 age provides a useful estimate of the climatological mean and seasonal properties of the (tropospheric) mean age (Waugh et al. (2013); Wu et al. (2018)), we emphasize that care must be taken when interpreting the long-term trends in Γ_{SF6} as reflecting (transport-related) trends in the age-of-air. A similar disconnect between the age trends inferred from SF_6 versus those derived from an age-of-air tracer was noted in Loeffel et al. (2021), albeit in the stratosphere, where the presence of mesospheric sinks in SF_6 can result in opposite trends between the two tracer-based ages.

Another novelty of our results relates to our use of a more spatially resolved reference times series used to calculate the SF_6 age. In particular, while model evaluation was not the main focus of this study, our use of a reference series that incorporates 31 (as opposed to 3) stations, reveals that the simulated spatial variance of SF_6 over northern midlatitudes is significantly larger than observed. We then demonstrated that this bias largely, but not entirely, accounts for the simulated age bias (∼0.3-0.4 years) in models over the southern extratropics, reported in previous studies (Waugh et al. (2013); Yang et al. (2019)). More precisely, after removing the influence of high SF_6 sites from the modeled reference time series used to calculate the age, we showed that the SF_6 age bias is reduced by ∼50%.

The presence of high SF_6 sites in the models may reflect either incorrect transport or emissions (or a combination of both). Focusing strictly on transport errors, these may be either related to mixing within the planetary boundary layer (Peters et al., 2004) or, as more recent studies have noted, to biases in the (resolved) near-surface meridional flow, even in simulations constrained with (re)analysis fields (Yang et al., 2019). A natural next step in this direction will be to examine in more detail the drivers of larger spatial variance of northern midlatitude SF_6 mixing ratios among the TransCom and CCMI models, which were all constrained with EDGAR v4.2 emissions. At the same time, inaccurate emissions distributions in the EDGAR inventory, especially over the United States, might also contribute to the simulated biases (Hu et al. (2021)). To this end, new targeted simulations modifying regional components of the EDGAR inventory may provide insight into how the simulated age biases respond to changes in emissions.

Finally, while our focus on trends and variability has primarily been on the surface, we have also used the aircraft measurements from ATom to investigate the vertical structure of Γ_{SF6}. Owing to measurement uncertainty and to the short record of the aircraft data, however, our ability to robustly quantify age trends and variability in the free troposphere has been quite limited. Nonetheless, model simulations suggest that there is considerable seasonal variability in Γ_{SF6} in the mid-to-upper troposphere over the Indian Ocean (Figure 5 in Wu et al. (2018)). While the lack of sufficient aircraft data from ATom currently limits our exploration of age variability over the Indian Ocean, the measurements obtained as part of future campaigns conducted over Asia may help in this endeavor. These may include measurements not only of SF_6, but also of volatile organic compounds and short-lived halogens with different lifetimes, which may be used in combination to constrain the transit time distribution (Holzer and Waugh (2015)). Future work, therefore, will focus on quantifying transport variability in both observations and models, particularly over the Asian monsoon region.

Acknowledgments

This research was supported by NASA's Atmospheric Composition Modeling and Analysis (ACMAP) Program. The authors thank the high-performance computing resources provided by NASA's Advanced Supercomputing (NAS) Division and the NASA Center for Climate Simulation (NCCS) as well as NASA's Modeling, Analysis and Prediction (MAP) program, which supports the core chemistry-climate and chemistry-modeling activities. The authors thank Sourish Basu (NOAA) and Lei Hu (NOAA) for constructive feedback. The NOAA/CCGG SF_6 surface flask data is available at https://gml.noaa.gov/ccgg/.

All ATom data used in this study can be accessed via https://daac.ornl.gov/ATOM/campaign/. The GMI model simulation output analyzed in this study can be publicly accessed at https://portal.nccs.nasa.gov/datashare/dirac/gmidata2/users/steenrod/tracers/.

References

Chen, G., Orbe, C., & Waugh, D. (2017). The role of monsoon-like zonally asymmetric heating in interhemispheric transport. *Journal of Geophysical Research: Atmospheres*, *122*(6), 3282–3298.

Denning, A. S., Holzer, M., Gurney, K. R., Heimann, M., Law, R. M., Rayner, P. J., et al. (1999). Three-dimensional transport and concentration of SF6: A model intercomparison study (TransCom 2). *Tellus B: Chemical and Physical Meteorology*, *51*(2), 266–297.

Elkins, J., Fahey, D., Gilligan, J., Dutton, G., Baring, T., Volk, C., et al. (1996). Airborne gas chromatograph for in situ measurements of long-lived species in the upper troposphere and lower stratosphere. *Geophysical Research Letters*, *23*(4), 347–350.

Elkins, J. W., Moore, F. L., & Kline, E. S. (2002). Update: New airborne gas chromatograph for NASA airborne platforms. In *Proceedings of the earth science technology conference* (pp. 1–3).

Eyring, V., Lamarque, J.-F., Hess, P., Arfeuille, F., Bowman, K., Chipperfiel, M. P., ... others (2013). Overview of IGAC/SPARC Chemistry-Climate Model Initiative (CCMI) community simulations in support of upcoming ozone and climate assessments. *SPARC newsletter*, *40*(Januar), 48–66.

Fahey, D. W., Churnside, J. H., Elkins, J. W., Gasiewski, A. J., Rosenlof, K. H., Summers, S., et al. (2006). Altair unmanned aircraft system achieves demonstration goals. *Eos, Transactions American Geophysical Union*, *87*(20), 197–201.

Frederiksen, J. S., & Francey, R. J. (2018). Unprecedented strength of hadley circulation in 2015–2016 impacts on CO2 interhemispheric difference. *Atmospheric Chemistry and Physics*, *18*(20), 14837–14850.

Gelaro, R., McCarty, W., Suárez, M. J., Todling, R., Molod, A., Takacs, L., ... others (2017). The modern-era retrospective analysis for research and applications, version 2 (MERRA-2). *Journal of climate*, *30*(14), 5419–5454.

Geller, L., Elkins, J., Lobert, J., Clarke, A., Hurst, D., Butler, J., & Myers, R. (1997). Tropospheric sf6: Observed latitudinal distribution and trends, derived emissions and interhemispheric exchange time. *Geophysical research letters*, *24*(6), 675–678.

Hall, B., Dutton, G., Mondeel, D., Nance, J., Rigby, M., Butler, J., ... Elkins, J. (2011). Improving measurements of SF6 for the study of atmospheric transport and emissions. *Atmospheric Measurement Techniques*, *4*(11), 2441–2451.

Hall, T., & Plumb, A. (1994). Age as a diagnostic of stratospheric transport. *Journal of Geophysical Research: Atmospheres*, *99*(D1), 1059–1070.

Hu, L., Montzka, S., DeCola, P., Dlugokencky, E., Ottinger, D., Bogle, S., et al. (2021). *Atmosphere-based US emission estimates of SF_6 for 2007-2018.* Retrieved from `https://meetingorganizer.copernicus.org/EGU21/EGU21-7980.html` (European Geophysical Union General Assembly)

Kida, H. (1983). General circulation of air parcels and transport characteristics derived from a hemispheric gcm part 2. very long-term motions of air parcels in the troposphere and stratosphere. *Journal of the Meteorological Society of Japan. Ser. II*, *61*(4), 510–523.

Lan, X., Hall, B., Dutton, G., Muhle, J., & Elkins, J. (2020). Atmospheric composition, long-lived greenhouse gases [in "State of the Climate in 2019"]. *Bulletin of the American Meteorological Society*, *101*(101 (8)), S70–S74.

Levin, I., & Hesshaimer, V. (1996). Refining of atmospheric transport model entries by the globally observed passive tracer distributions of 85krypton and sulfur hexafluoride (sf6). *Journal of Geophysical Research: Atmospheres*, *101*(D11), 16745–16755.

Levin, I., Naegler, T., Heinz, R., Osusko, D., Cuevas, E., Engel, A., et al. (2010). The global SF6 source inferred from long-term high precision atmospheric measurements and its comparison with emission inventories. *Atmospheric Chemistry and Physics*, *10*(6), 2655–2662.

Loeffel, S., Eichinger, R., Garny, H., Reddmann, T., Fritsch, F., Versick, S., et al. (2021). The impact of SF6 sinks on age of air climatologies and trends. *Atmospheric Chemistry and Physics Discussions*, 1–23.

Miyazaki, K., Patra, P. K., Takigawa, M., Iwasaki, T., & Nakazawa, T. (2008). Global-scale transport of carbon dioxide in the troposphere. *Journal of Geophysical Research: Atmospheres*, *113*(D15).

Moore, F., Elkins, J., Ray, E., Dutton, G., Dunn, R., Fahey, D., et al. (2003). Balloonborne in situ gas chromatograph for measurements in the troposphere and stratosphere. *Journal of Geophysical Research: Atmospheres*, *108*(D5).

Orbe, C., Waugh, D. W., Newman, P. A., & Steenrod, S. (2016). The transit-time distribution from the Northern Hemisphere midlatitude surface. *Journal of Atmospheric Sciences*, *73*(10), 3785–3802.

Orbe, C., Yang, H., Waugh, D. W., Zeng, G., Morgenstern, O., Kinnison, D. E., et al. (2018). Large-scale tropospheric transport in the Chemistry–Climate model Initiative (CCMI) simulations. *Atmospheric Chemistry and Physics*, *18*(10), 7217–7235.

Patra, P. K., Houweling, S., Krol, M., Bousquet, P., Belikov, D., Bergmann, D., et al. (2011). Transcom model simulations of CH4 and related species: linking transport, surface flux and chemical loss with CH4 variability in the troposphere and lower stratosphere. *Atmospheric Chemistry and Physics*, *11*(24), 12813–12837.

Patra, P. K., Takigawa, M., Dutton, G., Uhse, K., Ishijima, K., Lintner, B., ... others (2009). Transport mechanisms for synoptic, seasonal and interannual sf 6 variations and" age" of air in troposphere. *Atmospheric Chemistry and Physics*, *9*(4), 1209–1225.

Peters, W., Krol, M., Dlugokencky, E., Dentener, F., Bergamaschi, P., Dutton, G., ... Tans, P. (2004). Toward regional-scale modeling using the two-way nested global model TM5: Characterization of transport using SF6. *Journal of Geophysical Research: Atmospheres*, *109*(D19).

Simmonds, P. G., Rigby, M., Manning, A. J., Park, S., Stanley, K. M., McCulloch, et al. (2020). The increasing atmospheric burden of the greenhouse gas sulfur hexafluoride (SF6). *Atmospheric Chemistry and Physics*, *20*(12), 7271–7290.

Strahan, S., Douglass, A., & Steenrod, S. (2016). Chemical and dynamical impacts of stratospheric sudden warmings on Arctic ozone variability. *Journal of Geophysical Research: Atmospheres*, *121*(19), 11–836.

Strahan, S., Duncan, B., & Hoor, P. (2007). Observationally derived transport diagnostics for the lowermost stratosphere and their application to the GMI chemistry and transport model. *Atmospheric Chemistry and Physics*, *7*(9), 2435–2445.

Waugh, D., Crotwell, A., Dlugokencky, E., Dutton, G., et al. (2013). Tropospheric SF6: Age of air from the Northern Hemisphere midlatitude surface. *Journal of Geophysical Research: Atmospheres*, *118*(19), 11–429.

Wofsy, S. C. (2011). HIAPER Pole-to-Pole Observations (HIPPO): fine-grained, global-scale measurements of climatically important atmospheric gases and aerosols. *Philosophical Transactions of the Royal Society A: Mathematical, Physical and Engineering Sciences*, *369*(1943), 2073–2086.

Wu, X., Yang, H., Waugh, D. W., Orbe, C., Tilmes, S., & Lamarque, J.-F. (2018). Spatial and temporal variability of interhemispheric transport times. *Atmospheric Chemistry and Physics*, *18*(10), 7439–7452.

Yan, X., Konopka, P., Hauck, M., Podglajen, A., & Ploeger, F. (2020). Asymmetry and pathways of inter-hemispheric transport in the upper troposphere and lower stratosphere. *Atmospheric Chemistry and Physics Discussions*, 1–26.

Yang, H., Waugh, D. W., Orbe, C., Patra, P. K., Jöckel, P., Lamarque, J.-F., et al. (2019). Evaluating simulations of interhemispheric transport: interhemispheric exchange time versus SF_6 age. *Geophysical Research Letters*, *46*(2), 1113–1120.

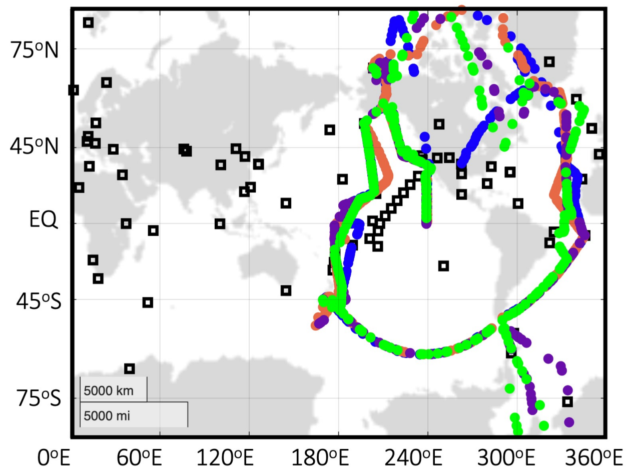

Figure 1. Map of locations of SF_6 surface measurements (NOAA/CCGG: black squares) and aircraft flights (filled circles) for ATom-1 (blue), ATom-2 (orange), ATom-3 (purple) and ATom-4 (green). Only the PFP merged aircraft data locations are shown, for sake of simplicity.

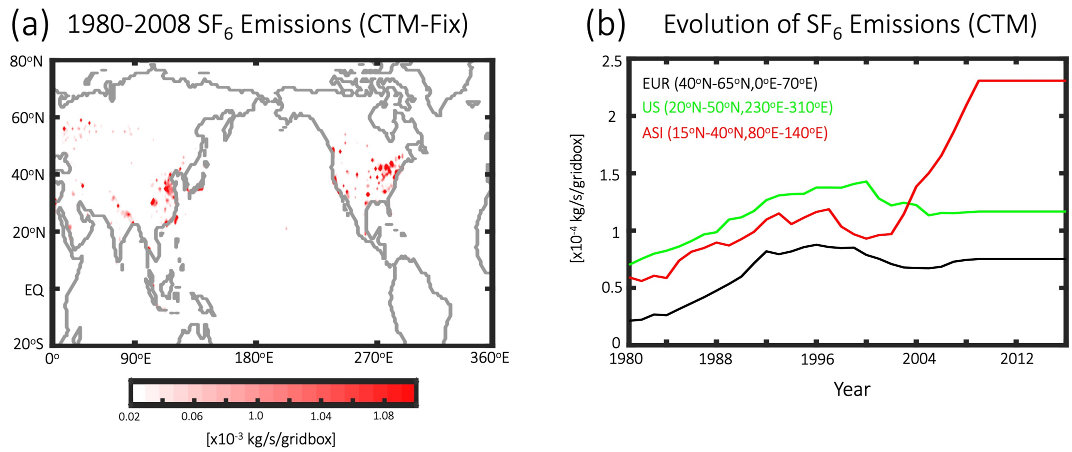

Figure 2. Map showing the climatological mean (1980-2008) Levin et al. (2010) emissions specified in the "CTM-Fix" simulation, which exhibit no shift from northern midlatitudes into northern subtropics over the 2000s. b) Temporal evolution of the EDGAR v4.2 emissions specified in the "CTM" simulation, averaged over the United States (green, US: 20°N-40°N, 230°E-310°E), Europe (black, EUR: 40°N-65°N, 0°E-70°E) and Asia (red, ASI: 15°N-40°N, 80°E-140°E). Note that any SH emissions represented in the Levin et al. (2010) and Edgar v4.2 inventories are not shown or visible in (a) as they are small (∼5%), relative to the emissions over the northern subtropics and midlatitudes.

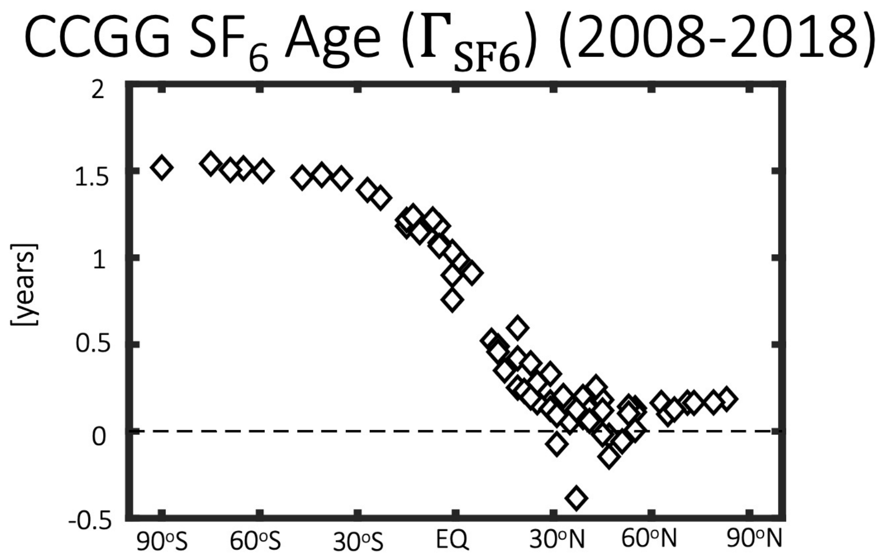

Figure 3. Meridional profile of the climatological mean observed SF_6 age (Γ_{SF6}), averaged over 2000-2018 and evaluated at all available NOAA/CCGG sites.

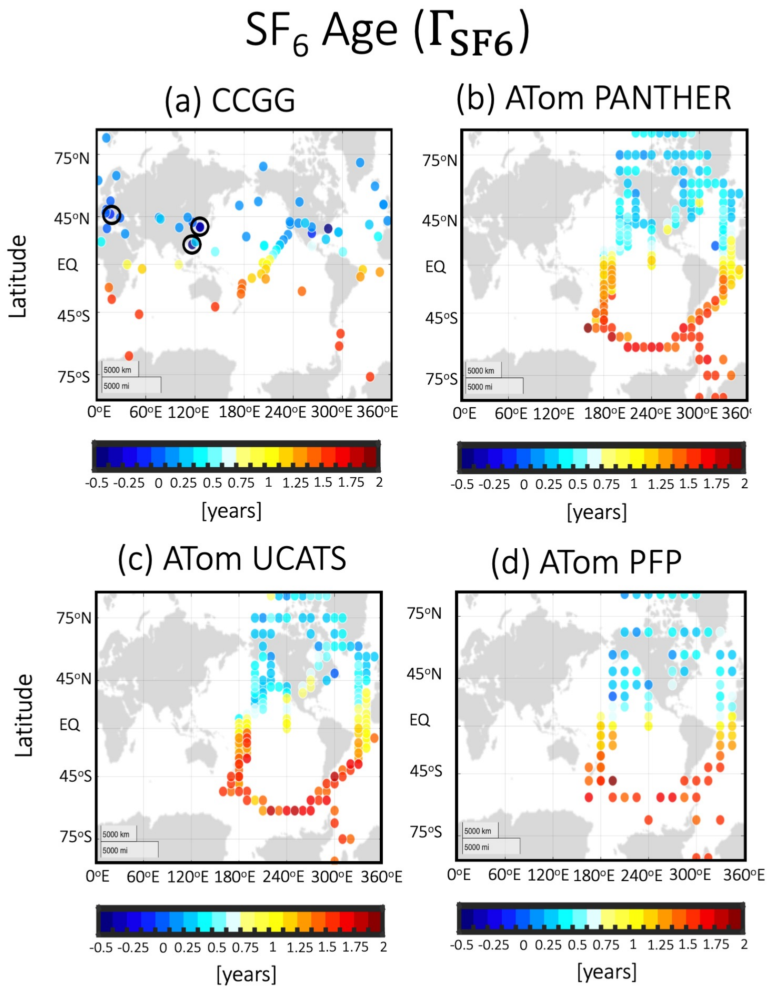

Figure 4. Climatological mean observed SF_6 age (Γ_{SF6}) derived from the NOAA/CCGG surface flask-air measurements (2008-2018) (a) and during ATom 1-4 for the PANTHER (b) and UCATS (c) instruments. Measurements are also shown from PFP (d), which consists of a package of flasks holding air samples that is analyzed separately from the ATom instrumentation. ATom-based ages have been averaged over pressures greater than 400 hPa; in addition, the PANTHER/UCATS and PFP measurements have been binned into a 10° longitude by 5° latitude and 15° longitude by 10° latitude grid, respectively, owing to the higher temporal sampling frequency for the former two instruments, compared to the latter. Black circles in (a) highlight sites over Europe (HUN) and Asia (DSI, TAP, AMY) where values of Γ_{SF6} are most negative and where changes in SF_6 emissions are important for interpreting age trends over the 2000s (see Figure 8). Note that the negative ages over the United States (at ITN (35°N,77°W)), which reflect measurements over a very limited time period (05/1997-05/1999), are not circled as they do not contribute to the trend analysis.

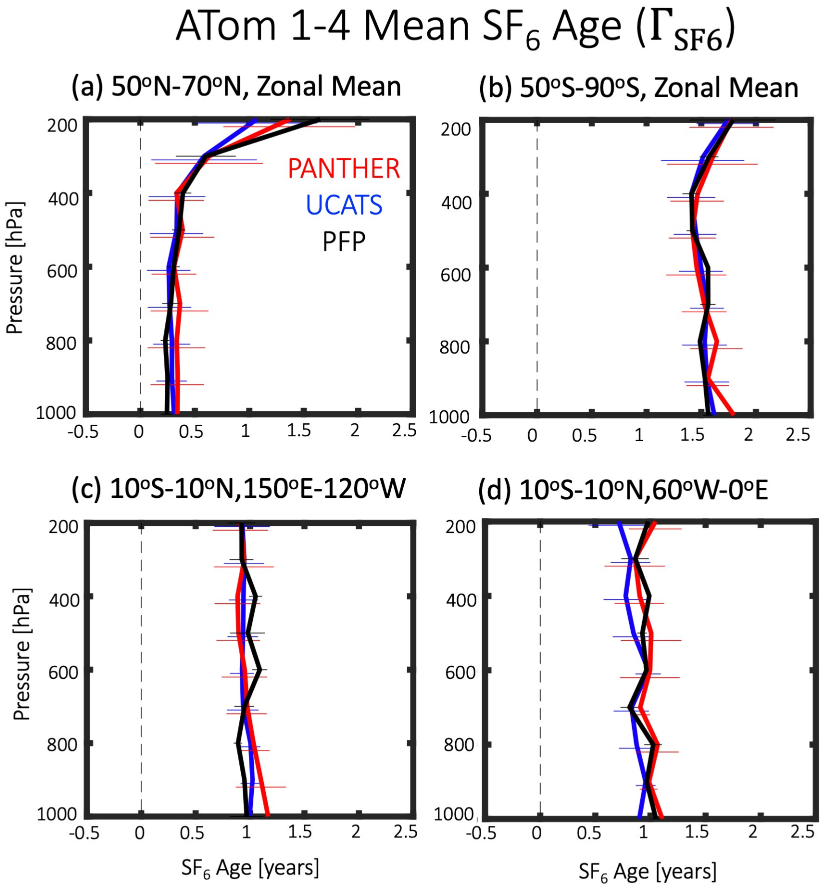

Figure 5. ATom 1-4 averaged Γ_{SF6} for the PANTHER (red), UCATS (blue) and PFP (black) measurements. Averages are presented over northern midlatitudes (a), southern middle and high latitudes (b) and the tropics over the Pacific (c) and Atlantic (d) oceans. Thin dashed lines indicate $\pm\sigma$ for each instrument, where σ is the standard deviation of all measurements sampled within each region.

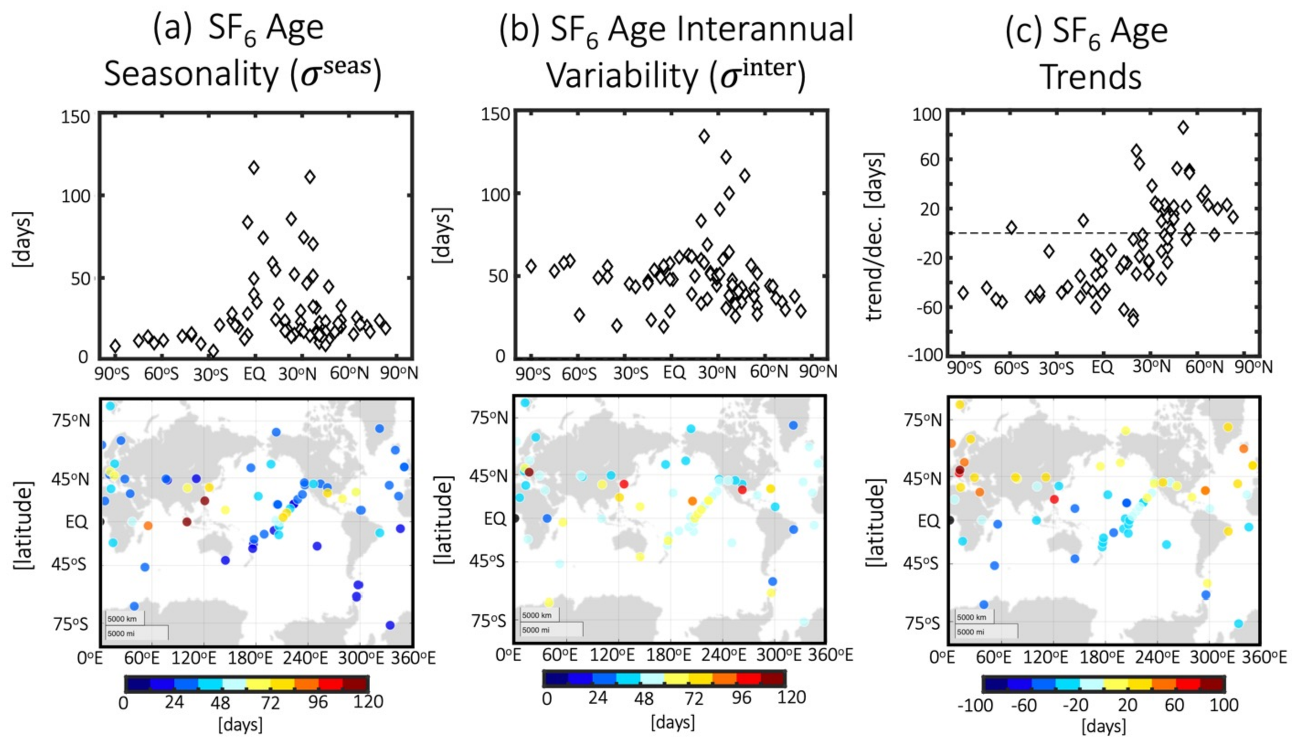

Figure 6. Variability and trends in observed SF_6 ages derived from the NOAA/CCGG SF_6 measurements. Left: Meridional profile of the seasonal variability (σ^{seas}) (top) and corresponding zonal variations (below). Middle: Meridional profile of the annual mean interannual variability (σ^{inter}) (top) and corresponding zonal variations (bottom), where the mean has been calculated using the interannual variability evaluated at each month. Bottom: Meridional profile of trends in Γ_{SF6} (top) over the observational period (2000-2018) and corresponding zonal variations (bottom).

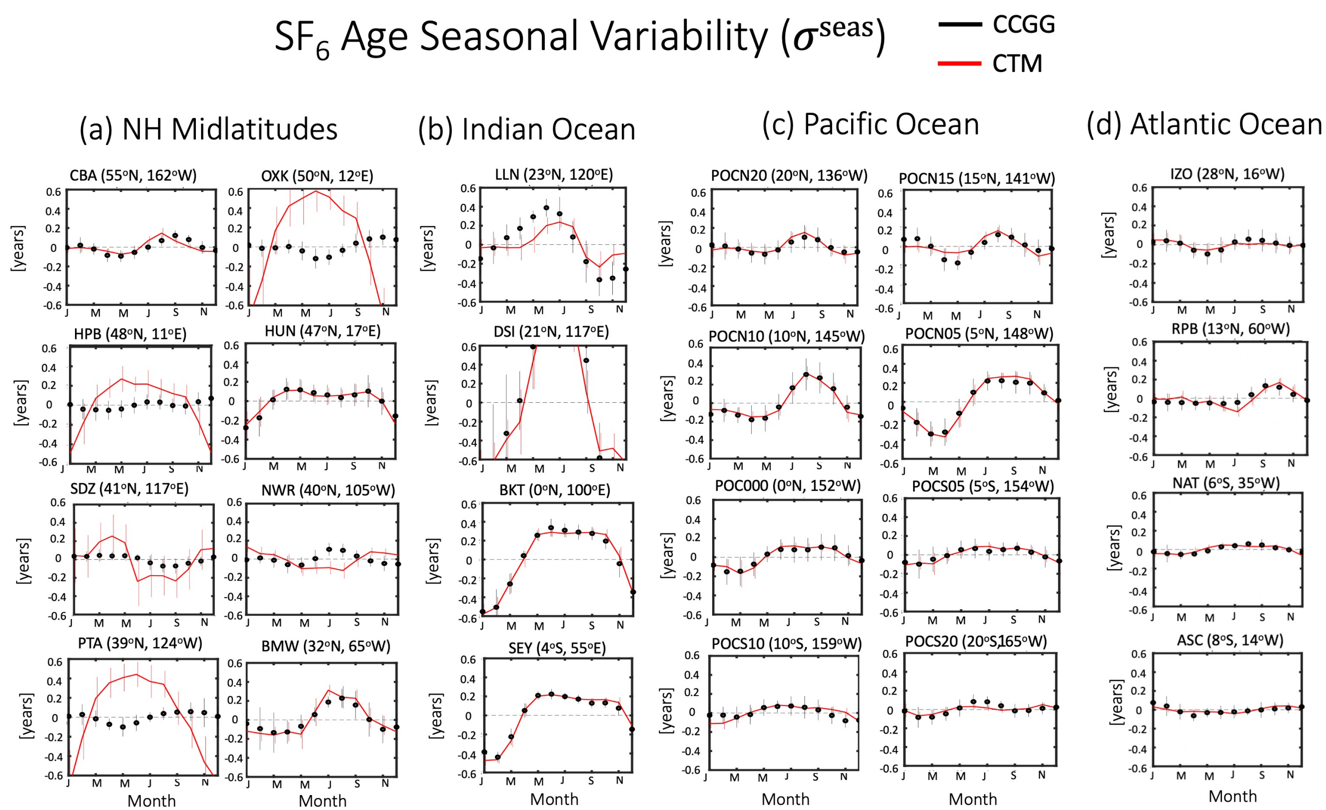

Figure 7. Seasonal cycle of Γ_{SF6}, evaluated at various northern midlatitude (a), Indian Ocean (b), Pacific Ocean (c) and Atlantic Ocean (d) sites for the observations (black) and the CTM simulation (red). Seasonality is evaluated over the entire observational period (1997-2018). Bars denote ± 1 annual standard deviation.

.

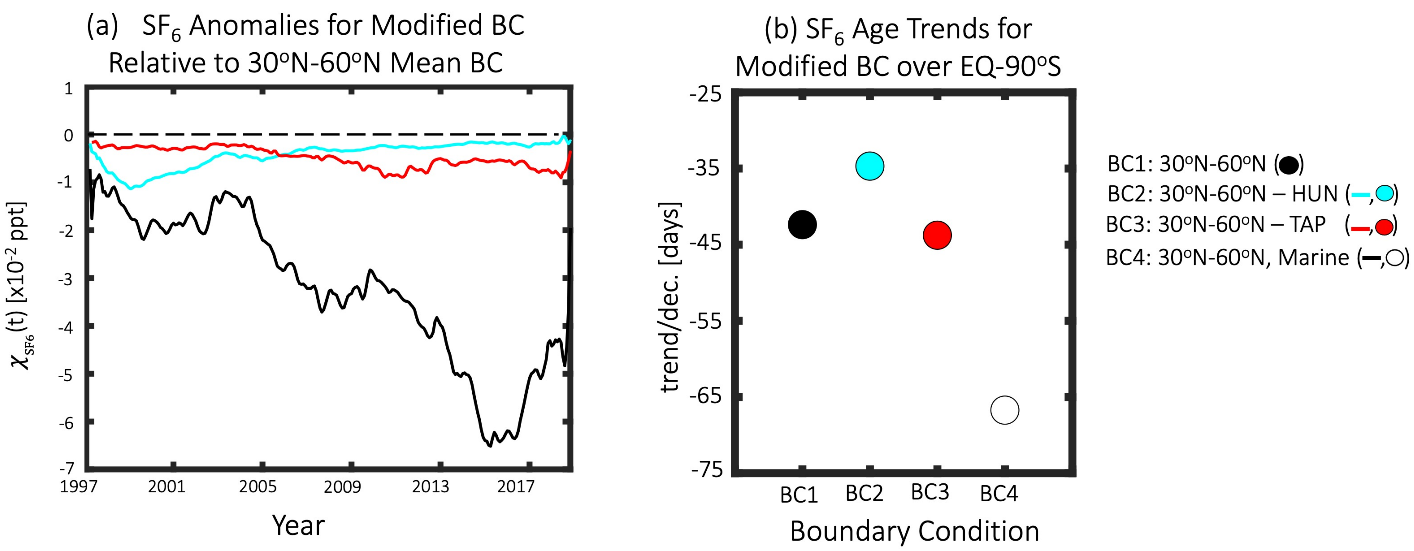

Figure 8. Sensitivity of observed SF_6 age trends over 2000-2018 to choice of boundary condition. Left: 23-month smoothed time series of SF_6 anomalies between the 30°N-60°N mean boundary condition (BC1) and boundary conditions that remove HUN (BC2, cyan), remove TAP (BC3, solid red), and remove all continental stations (BC4, solid black). Right: Comparisons of the EQ-90°N averaged Γ_{SF6} trends over 2000-2018 using BC1 (black, solid), BC2 (cyan), BC3 (red), and BC4 (black, open).

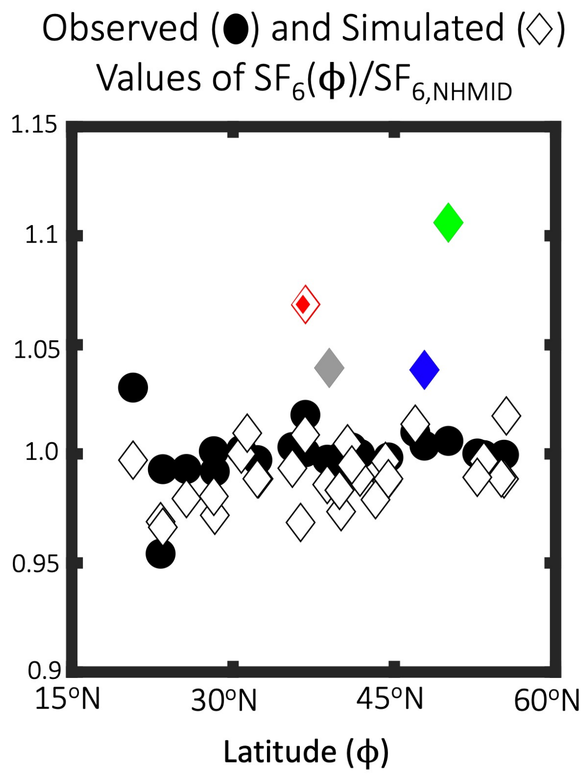

Figure 9. Ratio of SF_6 mixing ratio at individual sites, relative to the midlatitude (30°N-60°N) mean mixing ratio. The observed and simulated (CTM) values are shown in the black circles and diamonds, respectively. Also highlighted are the high-SF_6 sites in the model (TAP (red diamond), AMY (smaller red filled diamond), HPB (blue diamond), OXK (green diamond), PTA (grey diamond)). Note that the diamonds for the TAP and AMY sites overlap.

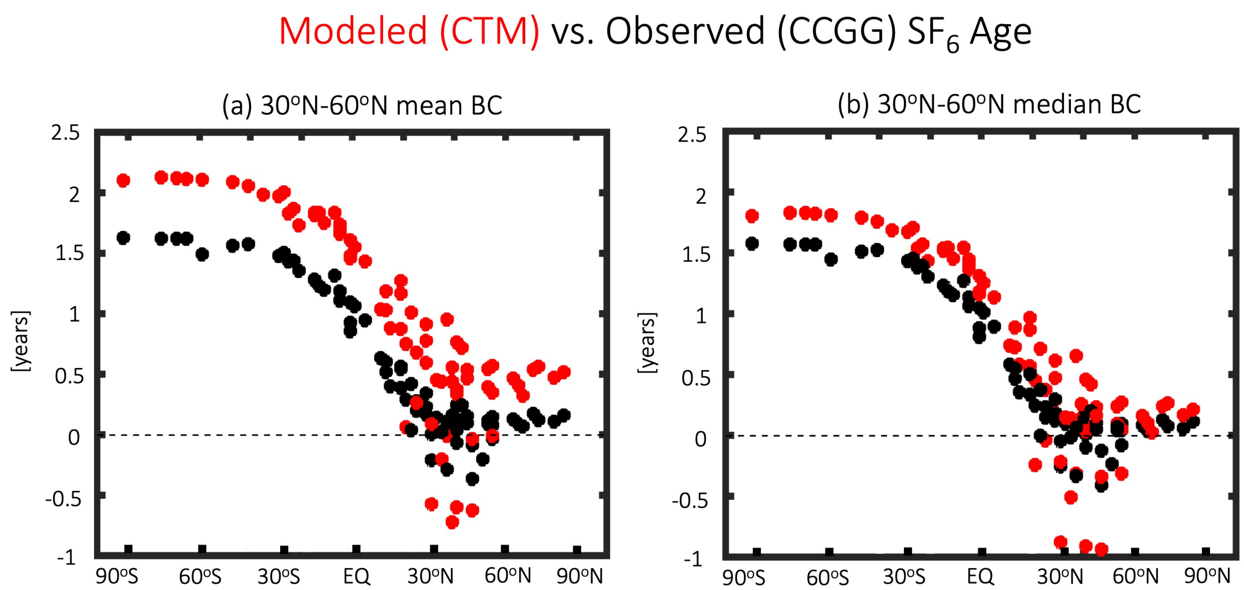

Figure 10. Comparisons of Γ_{SF6}, calculated using a reference SF_6 series based on the mean of all sites between 30°N and 60°N (a) versus the median (b). Observed and modeled values are shown in black and red, respectively. Climatological means are shown for years spanning 2000-2010. As in Figure 7 simulated values are taken from the CTM simulation but look similar for the CTM-Fix simulation (not shown).

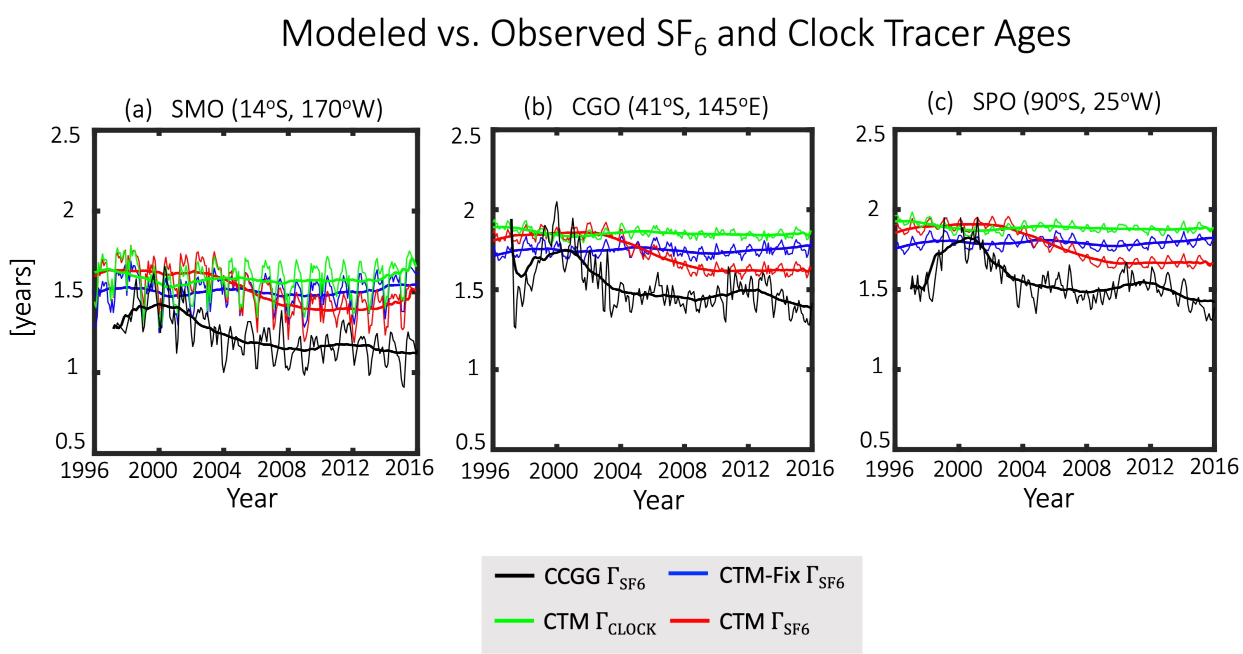

Figure 11. Time series of SF_6 ages at various Southern Hemisphere sites for the observations (black) and the CTM (red) and CTM-Fix (blue) simulations. The green line shows the clock tracer age (Γ_{clock}) for the CTM. The 23-month smoothed running mean is shown in the thick lines.

ATom	**Reported SF_6 Uncertainty PFP**	**Reported SF_6 Uncertainty UCATS**	**Reported SF_6 Uncertainty PANTHER**	**σ(PFP-UCATS)**	**σ(PFP-PANTHER)**	**σ(PANTHER-UCATS)**
1	0.05	0.11-0.13	0.05-0.11	0.13	0.09	0.13
2	0.05	0.05-0.07	0.05-0.10	0.08	0.11	0.11
3	0.05	0.05-0.12	0.05-0.10	0.08	0.10	0.11
4	0.05	0.06-0.09	0.07-0.15	0.11	0.10	0.11

Table 1. Table 1: Reported uncertainties (ppt) for the SF_6 measurements (col. 2-4) and the standard deviation (ppt) in the difference between coincident measurements (col. 5-7) sampled during ATom 1-4.